

# Efficient Equilibrium Testing under Adhesion and Anisotropy using Empirical Contact Force Models

Kris Hauser, *Member, IEEE*, Shiquan Wang, and Mark Cutkosky *Fellow, IEEE*

**Abstract**—This paper presents a method for efficiently testing the stability of an object under contact that accommodates empirical models of admissible forces at individual contact points. It handles a diverse range of possible geometries of the admissible force volume, including anisotropy, adhesion, and even non-convexity. The method discretizes the contact region into patches, performs a convex decomposition of a polyhedral approximation to each admissible force volume, and then formulates the problem as a mixed integer linear program. The model can also accommodate articulated robot hands with torque limits and joint frictions. Predictions of our method are evaluated experimentally in object lifting tasks using a gripper that exploits microspines to exert strongly anisotropic forces. The method is applied to calculate gripper loading capabilities and equilibrium predictions for a quadruped climbing robot on steep and overhanging terrain.

## I. INTRODUCTION

Contact force modeling is an essential component of grasp planning, physics simulation, end effector design, and biomechanics. The general purpose of such models is to simplify the countless microscopic interactions of a region of contact into a finite approximate representation that can be used for macroscopic predictions. Simple, mathematically convenient models like Coulomb friction are commonly used, but they fail to capture many phenomena including deformation, anisotropic friction, and adhesion, which are useful to exploit in engineering (e.g., novel surfaces [2, 14, 19] and micromanipulation [6]) as well as in understanding biological systems (e.g., the hairs on insect feet, Van der Waals forces on gecko feet, and claws on squirrels). To better characterize these complex interactions, empirical data can be used to capture the range of applicable forces during contact without slipping or separating [16, 26, 27]. Although data-driven techniques are useful for performance characterization and control of known systems, few methods are available to extrapolate contact force data to make computationally efficient predictions in novel scenarios.

This paper presents a computational method for testing static equilibrium of an object under empirical contact force models. Empirical material-material contact modeling is conducted with a simple force measurement procedure that captures a *force limit surface* describing the maximum forces exhibited by a small *contact unit* in any given direction. Then, for an object touched by a novel assembly of contact units, its equilibrium status under an external wrench is

K. Hauser is with the Departments of Electrical and Computer Engineering and of Mechanical Engineering and Materials Science, Duke University, Durham, NC, 27708 USA. S. Wang and M. Cutkosky are with the Department of Mechanical Engineering, Stanford University, Stanford, CA, 94305 USA. E-mail: kris.hauser@duke.edu, {shiquan,cutkosky}@stanford.edu.

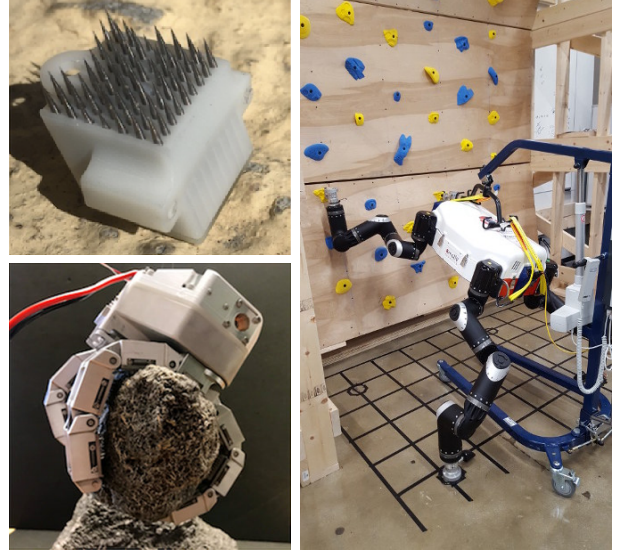


Fig. 1. The microspine unit used in this work (top left) uses spring-loaded needles to yield high effective friction on rough surfaces. Our method uses empirical measurements of its applicable contact forces to predict the maximum loading characteristics of the four-fingered SpinyHand gripper (bottom left). Loading estimates are then used to predict the feasibility of the Robosimian quadruped (right) climbing vertical terrain using these grippers.

predicted using a constrained optimization procedure. Unlike past work which largely assumes that valid contact forces are limited to conic and/or convex regions, this paper interested in supporting calculations with non-convex regions. To handle non-convexity, a mixed-integer linear programming (MILP) approach is presented that performs a branch-and-bound (BnB) using a hierarchical convex decomposition. The method is globally optimal and significantly faster than off-the-shelf MILP solvers. The basic method is also extended to account for constraints in articulated robots, such as joint frictions, torques, and springs.

Experiments are conducted on a microspine unit that uses spring-loaded needles oriented at an angle to achieve high lateral loads on rocky surfaces [2, 24]. When pressed against a rough surface, several needles engage with asperities (indentations) on the surface leading to very large effective friction and slightly adhesive properties. We apply our method to design microspine grippers that handle objects with a given geometry and load. Specifically, we evaluate the loading capabilities of a gripper at a given contact and finger configuration (Fig. 1). We compute wrench spaces for a variety of gripper configurations, and experiments show that even on problems of relatively modest size, the novel algorithm outperforms standard MILP

solvers by one or more orders of magnitude. Finally, we employ the calculated gripper wrench spaces in a hierarchical manner to efficiently test the equilibrium of the body of a climbing quadruped robot in arbitrary postures and grips.

## II. RELATED WORK

The standard Coulomb friction point contact model is mathematically convenient, and allows for accurate and fast computational methods that predict many aspects of behavior between rigid objects in contact, such as force closure, optimal forces to resist an external wrench, static equilibrium, and dynamic simulation [3, 4, 5, 7, 20, 22]. Mathematically, Coulomb friction may be expressed as a cone constraint, which leads to linear constraints in 2D or second-order cone constraints in 3D. A variety of conic extensions to the Coulomb model have been proposed, including a soft-finger approximation, polyhedral approximations, and anisotropic friction with elliptical constraints [3, 4]. However, these contact representations do not accurately represent continuous pressure distributions across a contact surface, and suffer from difficulties in model selection and parameter identification [17]. Data-driven approaches have been investigated in recent work to overcome many of the limitations of analytic models [9, 26, 27]. These approaches use extensive instrumentation and lengthy data gathering procedures to capture thousands or millions of force and motion readings. In contrast, the method presented in this paper combines both analytical and empirical approaches by extending empirical force limit surface measurements with rigid body mechanics, and is able to make physically validated macroscopic predictions with a modest amount of data.

Limit surfaces were introduced as a description of forces exerted on objects during planar sliding [11] and frictional contact [18] that are amenable to empirical testing. Recent work used polynomial level set representations of limits surfaces and identified parameters from empirical data using sum of squares methods [27]. Similar empirical testing has been used to model soft finger contact [8, 23]. Novel devices that may be amenable to such modeling techniques include directional adhesive materials [15] and microspines [2]. More related to our work is Hawkes et al. [15], who use the limit surface of one adhesion unit to predict the feasibility of loading directions for two- and three-unit devices. However it does not handle non-convexity in the admissible force volume nor propose a computational method for general equilibrium prediction.

This paper is an extended version of a conference paper [13] that includes more details about the optimization technique and an entirely new section on hierarchical equilibrium testing.

## III. EQUILIBRIUM WITH EMPIRICAL FORCE MODELS

The general framework for our method is as follows:

- 1) Acquire limit surfaces defined locally with respect to a canonical surface-centric reference frame.
- 2) For a novel contact situation, estimate the contact region and split it into a finite number of contact patches. This yields a *contact assembly*.

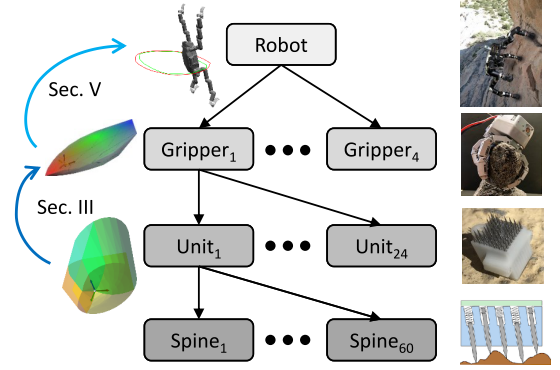


Fig. 2. Schematic of the hierarchical equilibrium prediction technique employed in this paper. Force limit surfaces of microspine units are used to predict wrench limit surfaces for grippers, which are in turn used to predict equilibrium of the legged robot.

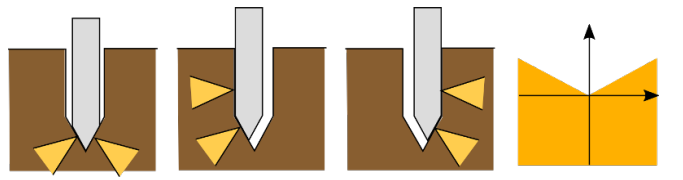


Fig. 3. Non-convex admissible force volumes (right) can arise out of micro-interactions. Consider a peg-in-hole setup where the peg makes frictional contact with different sides of the hole depending on the external loading condition. Friction leads to apparent adhesion when shear loads are applied.

- 3) Compute equilibrium prediction for the assembly under the estimated external wrench.

We will focus primarily on steps 1 and 3, and assume that the information in step 2 is provided through some other channels such as sensors or prior knowledge. In this section, we focus on predicting loading capabilities of grippers from small units. We extend this in a hierarchical manner to body equilibrium prediction in Sec. V (Fig. 2).

### A. Contact Model

A contact region  $C$  between bodies  $O_A$  and  $O_B$  is modeled as a rigid surface with a normal direction  $n$  defined at each point  $x \in C$ . To handle anisotropy of friction forces, two orthogonal vector fields  $u$  and  $v$  are defined over  $C$ , which defines an orthogonal frame  $R = (u, v, n)$  at all points  $x \in C$ . The region is discretized into a finite number of *contact patches*  $p_1, \dots, p_k$ . Each patch  $i = 1, \dots, k$  is centered at the point  $x_i$  and is associated with frame  $R_i$ .

At each contact patch, an *admissible force volume*  $F_i \subseteq \mathbb{R}^3$  describes the set of valid forces  $f_i$  applied to object  $O_B$  at each point  $x_i$ . This volume is defined as the interior of the force limit surface  $f_{max}(d) : S^2 \rightarrow [0, \infty)$  which describes the maximum force in every direction in 3D. In other words  $F_i = \{f \in \mathbb{R}^3 \mid \|f\| \leq f_{max}(\hat{f})\}$  where  $\hat{f} = f/\|f\|$  is the unit vector in the direction of  $f$ . The world-oriented admissible force volume is a rotation of a *local limit surface* rotated by the frame  $R_i$ .

We measure a local limit surface described with respect to a canonical 3D reference frame aligned with  $R = (u, v, n)$ . For a given pair of materials, the local limit surface value in

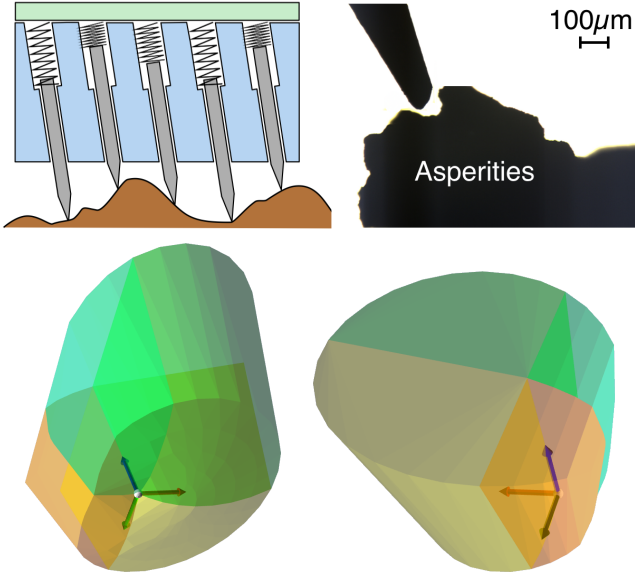


Fig. 4. Top: Diagram of a linearly-constrained microspine unit (left) and microscopic view of a spine about to catch on asperities (right). Bottom: two views of the admissible force volume for the microspine unit used in this work. Colors indicate different components of the volume's convex decomposition. Axes are labeled as follows:  $x$  (red) the shear direction,  $y$  (green) the lateral tangent direction, and  $z$  (blue) the normal direction pointing into the unit. (Figure best viewed in color)

a given direction  $d$  can be measured using a force sensor by applying a directional force to one object, keeping the other fixed, until the interface slips or otherwise breaks contact. For inward-pointing (compressive) directions,  $f_{max}(d)$  can either be infinite or capped by a maximum force that does not damage the object. For outward-pointing (separating) directions,  $f_{max}(d)$  will be 0 in the absence of adhesion. This process is repeated for a large number of directions. More details about this measurement procedure will be presented in Sec. IV-A.

Although the limit surface is a normally-displaced sphere, the admissible force volume may be non-convex, and we are particularly interested in handling these situations. Non-convexity occurs in the case of surfaces that have multiple points of irregular micro-contact (Fig. 3), which can cause them to exhibit exotic adhesive behavior such as the microspine units presented below (Fig. 4). There may also be non-convex behavior in the compressive limits of buckling internal structures, such as corrugated cardboard which are stiffer in directions not parallel to the normal.

### B. Equilibrium Testing

Equilibrium testing asks whether an external wrench  $w_{ext} \equiv (f_{ext}, t_{ext}) \in \mathbb{R}^6$  applied to  $O_B$  can be resisted by forces at the contact points. Assume  $t_{ext}$  is the external torque about the origin. Often, the external wrench is due only to gravity, the center of mass of  $O_B$  is taken to be the origin, and hence  $f_{ext} = mg$  and  $t_{ext} = 0$ . Three conditions must be met for equilibrium to hold: force balance, torque balance, and admissibility of contact forces. In other words, it seeks a

solution to the following feasibility problem:

Find  $f_1, \dots, f_k$  such that

$$\begin{aligned} \sum_{i=1}^k f_i + f_{ext} &= 0 \\ \sum_{i=1}^k x_i \times f_i + t_{ext} &= 0 \\ f_i &\in F_i \text{ for } i = 1, \dots, k \end{aligned} \quad (1)$$

For notational convenience, define the wrench matrix

$$W = \begin{bmatrix} I & I & \cdots & I \\ [x_1] & [x_2] & \cdots & [x_k] \end{bmatrix} \quad (2)$$

where  $[v]$  denotes the skew-symmetric cross product matrix, and define  $\mathbf{f} = (f_1, \dots, f_k)$  as the vector of contact forces. Problem (1) can then be expressed more compactly as

Find  $\mathbf{f}$  such that

$$W\mathbf{f} + w_{ext} = 0 \quad (3)$$

$$f_i \in F_i \text{ for } i = 1, \dots, k.$$

To solve this problem efficiently and exactly when all of the  $F_i$  are convex polyhedral regions, a linear program (LP) can be solved. This LP has  $3n$  variables and  $6 + nk$  constraints where  $k$  is the number of faces bounding each  $F_i$ . However, alternative techniques are needed to solve the case of non-convex regions.

### C. Joint torques

To apply this method to an articulated robot, we enforce static equilibrium of forces and joint torques. This functionality is useful for determining whether equilibrium holds in the presence of passive joints or torque limits.

Let  $O_A$  be the robot at configuration  $q$  and  $O_B$  be the object. Given the effects of gravity and a set of forces  $f_1, \dots, f_k$  that yield static equilibrium with  $O_B$ , the robot's joint torques  $\tau$  must obey the following equilibrium balance equation:

$$G(q) = \tau - \sum_{i=1}^k J_i(q)^T f_i \quad (4)$$

where  $G(q)$  is the generalized gravity vector and  $J_i$  is the Jacobian of the  $i$ 'th contact point. Note the introduction of the negative sign because the forces act on the object, while the equal and opposite force acts on the robot.

If sufficient torque were always available to the robot to enact the desired equilibrium balance, the force vector  $\mathbf{f}$  could be solved independently from the torques, and torques calculated from (4). However, in the presence of torque limits, it may not be possible to enact such torques for a given solution  $\mathbf{f}$ , whereas contact force indeterminacy might allow for valid torques for some other solution  $\mathbf{f}'$ .

As a result we incorporate torque limits  $\tau_{min} \leq \tau \leq \tau_{max}$  (inequalities taken element-wise) into constraints on  $\mathbf{f}$  as follows:

$$\tau_{min} \leq G(q) + \sum_{i=1}^k J_i(q)^T f_i \leq \tau_{max}. \quad (5)$$

For fixed  $q$  these inequalities are linear in  $\mathbf{f}$ .

#### D. Wrench-space limit surface calculation

A useful procedure for design of grasps and fixtures is to calculate the contact arrangement's wrench space  $\mathcal{W}$ .  $\mathcal{W}$  is defined as the subset of wrenches  $w_{ext} \in \mathbb{R}^6$  that can be resisted in equilibrium by admissible forces according to (3). We note that this is not necessarily a convex set. But it is apparent that for any point  $w \in \mathcal{W}$ , we can say that  $cw \in \mathcal{W}$  for all  $c \in [0, 1]$ . In other words, in order to determine  $\mathcal{W}$  it suffices to calculate its limit surface  $\partial\mathcal{W}$ .

To do so we employ a method to optimize the external wrench in a given 6D direction such that equilibrium is maintained. Specifically, given some unit direction  $\hat{w} \in \mathbb{R}^6$ , a new variable  $d$  is introduced into (3). Rather than only finding the contact force vector,  $d$  is maximized subject to the equality constraint  $w_{ext} = d\hat{w}$ , i.e., we solve

$$\begin{aligned} & \max_{\mathbf{f}, d} d \\ & W\mathbf{f} + d\hat{w} = 0 \\ & f_i \in F_i \text{ for } i = 1, \dots, k. \end{aligned} \quad (6)$$

Then, the limit surface can be obtained by sweeping  $\hat{w}$  about the unit sphere in 6D,  $S^5$ . In practice, to avoid requiring a excessive number of points, it can be more effective to approximate the wrench space by calculating its extents along different subspaces. Then  $\mathcal{W}$  can be approximated as the intersection of the cylindrical extrusion of these extents back into 6D space.

#### E. Separation Direction Prediction

In the case that equilibrium does not hold, it may be valuable to predict which contact patches will separate and how the object will behave upon separation. Hence, we propose testing an alternative formulation that uses the maximum dissipation principle, which posits that frictional forces are determined to minimize the post-contact second derivative of kinetic energy of the system. This derivative is  $\frac{d^2}{dt^2}(\frac{1}{2}\dot{q}^T B \dot{q}) = \frac{d}{dt}(\dot{q}^T B \ddot{q}) = \ddot{q}^T B \ddot{q} + \dot{q}^T B \ddot{q} = \dot{q}^T B \ddot{q}$  where the last equality holds because  $\ddot{q} = 0$ . Hence, this condition seeks

$$\begin{aligned} & \min_{\mathbf{f}} \ddot{q}(\mathbf{f})^T B \ddot{q}(\mathbf{f}) \\ & NW^T \ddot{q}(\mathbf{f}) \geq 0 \\ & f_i \in F_i \text{ for } i = 1, \dots, k \end{aligned} \quad (7)$$

where  $\ddot{q}(\mathbf{f}) \in \mathbb{R}^6$  is the post-forcing acceleration and angular acceleration (twist rate) of  $O_B$ ,  $B$  is the  $6 \times 6$  mass matrix of the object, and  $N$  is the  $n \times 3n$  block matrix of normal directions at each contact point  $diag(n_1^T, \dots, n_k^T)$ . We express  $\ddot{q}(\mathbf{f})$  as

$$\ddot{q}(\mathbf{f}) = B^{-1}(W\mathbf{f} + w_{ext}). \quad (8)$$

Hence, if all the  $F_i$  are convex polytopes, then (7) can be solved exactly as a convex quadratic program.

#### F. Branch-and-bound equilibrium solver

We are now ready to present our primary contribution, which is a method for handling non-convex admissible force volumes in problem (3), with optional constraints (5). Given that these problems can be solved via a convex program

when given convex admissible force volumes, we proceed by computing a convex decomposition of each of the  $F_i$ , and formulating a mixed integer linear program (MILP). First, we present the method in the simpler context of equilibrium testing (3), which asks for the first feasible solution.

Suppose each of the  $k$  force volumes is decomposed into  $c$  components,  $F_i = F_{i,1} \cup \dots \cup F_{i,c}$  where each  $F_{i,j}$  is a convex polyhedron. Here  $c$  is considered constant over each  $i$  purely for simplicity of notation; in general it is allowed to vary. With each component given by a set of halfplanes  $F_{i,j} \equiv \{f \in \mathbb{R}^3 \mid A_{i,j}f \leq b_{i,j}\}$ , we formulate a MILP with  $ck$  indicator variables  $z_{i,j} \in \{0, 1\}$  as follows:

$$\begin{aligned} & \text{Find } \mathbf{f}, z_{1,1} \dots z_{k,c} \text{ such that} \\ & W\mathbf{f} + w_{ext} = 0 \\ & A_{i,j}f_i \leq b_{i,j} + M(1 - z_{i,j}) \text{ for } i = 1, \dots, k \text{ and } j = 1, \dots, c \\ & z_{i,j} \in \{0, 1\} \text{ for all } i, j \\ & \sum_{j=1}^c z_{i,j} = 1 \text{ for all } i \end{aligned} \quad (9)$$

where  $M$  is some large number (e.g., larger than the maximum radius of any force volume). Each of the indicators, when 1, activates the constraints of the corresponding convex component. However, solving this MILP is usually prohibitively expensive because it is large (more than 10,000 constraints in many of our test problems) and may require exploring up to  $c^k$  integer solutions, which is  $7.9 \times 10^{28}$  in our largest problem with  $c = 4$  and  $k = 48$ . As a result we use a BnB method, with a convex bounding volume hierarchy to speed up the search.

The general idea is to maintain for each  $F_i$  a bounding volume hierarchy (BVH) consisting of a tree  $T_i$  of convex volumes, whose leaves are the components of the convex decomposition  $F_{i,1}, \dots, F_{i,c}$ . Each parent node stores the convex hull of all of its children, and hence the root node of  $T_i$  stores  $hull(F_i)$ .

Let  $S_i$  denote a node in  $T_i$ , and let  $(S_1, \dots, S_k)$  be a state consisting of combinations of nodes. Define  $CP(g, S_1, \dots, S_k)$  as the convex program (3) relaxed by replacing each  $F_i$  with  $hull(S_i)$ , and using the objective function  $g$ . The algorithm recurses over states as follows:

```

1: procedure BNB-EQ
2:   Let  $S_i$  be the root of  $T_i$  for  $i = 1, \dots, k$ 
3:   return Eq-recurse( $S_1, \dots, S_k$ )
4:
5: procedure EQ-RECURSE( $S_1, \dots, S_k$ )
6:   Solve  $\mathbf{f} \leftarrow CP(g, S_1, \dots, S_k)$ 
7:   If  $\mathbf{f} = nil$ , then return  $nil$   $\triangleright$  No solution in subtrees
8:   Otherwise, let  $(f_1, \dots, f_k) = \mathbf{f}$ 
9:   if  $f_i \in F_i$  for all  $i = 1, \dots, k$  then return  $\mathbf{f}$ 
10:  Let  $j \leftarrow \arg \max_i dist(f_i, F_i)$   $\triangleright$  Ordering heuristic
11:   $C_1, C_2 \leftarrow Children(S_j)$ 
12:  if  $dist(f_j, C_2) < dist(f_j, C_1)$  then
13:    Swap  $C_1$  and  $C_2$ 
14:   $\mathbf{f} \leftarrow$  Eq-recurse( $S_1, \dots, S_{j-1}, C_1, S_{j+1}, \dots, S_k$ )
15:  if  $\mathbf{f} \neq nil$  then return  $\mathbf{f}$ 
```

```

12:    $\mathbf{f} \leftarrow \text{Eq-recurse}(S_1, \dots, S_{j-1}, C_2, S_{j+1}, \dots, S_k)$ 
13:   if  $\mathbf{f} \neq \text{nil}$  then return  $\mathbf{f}$ 
14:   return  $\text{nil}$ 

```

In Line 3, there is no possible solution to any combination of leaves under  $S_1, \dots, S_k$ , so the node is pruned. In Line 5, the relaxed solution is a solution to the original problem. In Lines 6–13, the relaxed solution lies in a concavity, so branching is needed. To minimize the amount of branching, we use three heuristics:

- The BVH minimizes the deviation between a convex volume and the subset of  $F_i$  contained therein.
- Only the node  $S_i$  of a single tree is selected for branching. The node and the order in which children of  $S_i$  are tested are determined through heuristics described below.
- The objective function  $g$  is constructed to prefer solutions close to the centroids of each of the  $S_i$ 's.

These are described in more detail below.

a) *BVH construction*: We use a bottom up approach. First, let the convex decomposition of a polyhedral set  $A$  be given as  $A_1, \dots, A_c$ . For each pair of components  $A_i$  and  $A_j$  the hull  $B_{i,j} = \text{hull}(A_i \cup A_j)$  and its volume measure  $\mu(B_{i,j})$  are computed. The pair that minimizes the excess  $\mu(B_{i,j}) - \mu(A_i) - \mu(A_j)$  is chosen for merging. Then, both components are removed from consideration, and the process repeats until all items are merged. Merging rounds are repeated recursively until only the root remains.

b) *Branch ordering heuristics*: The branched subtree  $S_j$  selected in Line 6 maximizes the distance from the relaxed force  $f_j$  to  $F_j$  (if  $f_j \in F_j$ , then  $\text{dist}(f_j, F_j) = 0$ ). Its children are also tested in order of increasing distance.

c) *Objective function heuristics*: To maximize the likelihood of  $CP(g, S_1, \dots, S_k)$  finding a solution that is admissible (i.e., early exit in Line 5), the objective function is designed to prefer forces respectively near the centroids of the union of the components in the leaves under  $S_1, \dots, S_k$ . Specifically, for each  $i = 1, \dots, k$  we find the union of components in the leaves of  $S_i$ , and compute its centroid  $c_i$ . Then, the objective function is defined as the L- $p$  norm

$$g(\mathbf{f}) = \sum_{i=1}^k \|f_i - c_i\|_p \quad (10)$$

with  $p$  either 1, 2, or  $\infty$ . In the case of  $p = 2$ , the problem becomes a quadratic program which is a bit more computationally expensive than an LP, so we typically prefer  $p = 1$  or  $p = \infty$ .

#### G. Branch-and-bound optimizer

In optimization problems like (7) and calculating the wrench space of an assembly, the first valid solution may not be optimal. Hence, an alternate BnB is used for these tasks.

Let  $g^*$  be the optimal value of the objective function  $g(\mathbf{f})$ . The algorithm maintains a known upper bound  $\bar{g} \geq g^*$ , and  $\bar{g}$  is progressively lowered by traversing subsequently finer states. Since a non-leaf state describes a relaxed optimization problem, its optimum is a lower bound on the value of  $g(\mathbf{f})$

over all feasible values of  $\mathbf{f}$  beneath that leaf. Hence, we use these lower bound values to sort a priority queue. Pseudocode is listed below.

```

1: procedure BNB-OPT( $g, \epsilon$ )
2:   Let  $S_i$  be the root of  $T_i$  for  $i = 1, \dots, k$ 
3:    $Q \leftarrow$  empty priority queue
4:    $\text{push}(Q, (S_1, \dots, S_k), 0)$ 
5:    $\bar{g} \leftarrow \infty$ 
6:   while  $Q$  is not empty do
7:      $(S_1, \dots, S_k) \leftarrow \text{pop-min}(Q)$ 
8:     Solve  $\mathbf{f} \leftarrow CP(g, S_1, \dots, S_k)$ 
9:     If  $\mathbf{f} = \text{nil}$ , then return to Step 6
10:    Let  $(f_1, \dots, f_k) = \mathbf{f}$ , and  $g_f = g(\mathbf{f})$ 
11:    if  $g_f + \epsilon(1 + |g_f|) \geq \bar{g}$  then return to Step 6
12:    if  $f_i \in F_i$  for all  $i = 1, \dots, k$  then
13:       $\bar{g} \leftarrow g_f$             $\triangleright$  Best feasible solution so far
14:    else
15:       $\triangleright$  Early upper bound determination
16:       $L_1, \dots, L_k \leftarrow \text{rand-leaves}(\mathbf{f})$ 
17:      Solve  $\mathbf{f} \leftarrow CP(g, L_1, \dots, L_k)$ 
18:      If  $\mathbf{f} \neq \text{nil}$  then  $\bar{g} \leftarrow \min \bar{g}, g(\mathbf{f})$ 
19:     $\triangleright$  Splitting
20:    Let  $j \leftarrow \arg \max_i \text{dist}(f_i, F_i)$ 
21:     $C_1, C_2 \leftarrow \text{Children}(S_j)$ 
22:     $\text{push}(Q, (S_1, \dots, S_{j-1}, C_1, S_{j+1}, \dots, S_k), g_f)$ 
23:     $\text{push}(Q, (S_1, \dots, S_{j-1}, C_2, S_{j+1}, \dots, S_k), g_f)$ 
24:   return  $\bar{g}$ 

```

Recursion under the current state is pruned in Line 9 if there is no solution, and in Line 11 if it has no chance of containing an optimal solution. This is because since  $g_f$  is a lower bound on the optimal value of all combinations of leaves under  $S_1, \dots, S_k$ . In Line 12–13, the relaxed solution is an optimal solution below the current state. Otherwise, Line 15–21 splits a tree, chosen again using the maximum distance heuristic.

To reduce the upper bound quickly, *early upper bound determination* in Lines 15–17 calculate the optimal forces at a fully-determined set of leaf nodes in the hope of finding a better solution. To do so, for each subtree  $S_i$  we pick a leaf such that if  $f_i \in F_i$ , the leaf is set to the component in which  $f_i$  is contained, and if  $f_i \notin F_i$ , a random leaf is chosen.

An exact solution would be found by using  $g_f \geq \bar{g}$  in Line 11. However, this can lead to excessive run times in the presence of numerical errors, and when redundancy in internal forces allows many optimal solutions amongst combinations of components. Hence, we allow a *relaxed optimality condition* with suboptimality factor of  $\epsilon(1 + |g^*|)$ , where  $\epsilon \geq 0$  is a user-defined parameter (set to 0.001 in our experiments).

## IV. EQUILIBRIUM TESTING EXPERIMENTS

This section presents numerical and physical experiments on several gripping devices based on microspine units. Experiments are conducted to characterize the unit's contact properties and test the stability of passive grasps with these grippers under a variety of configurations and surface conditions.

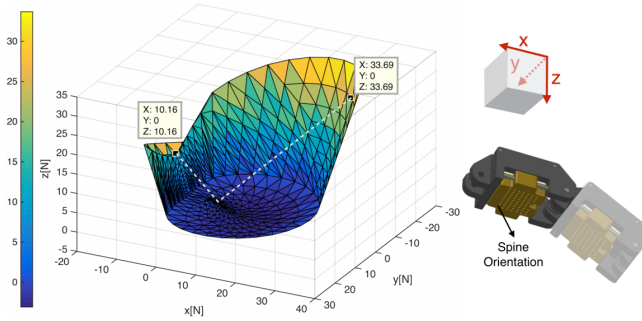


Fig. 5. Local limit surface (left): lumped contact property of the micro-spine unit on each gripper phalanx. The coordinate frame (upper right) is consistent with the assumed coordinate convention (lower right).

### A. Microspine Unit Modeling

Microspines are hooks or needles with very sharp tips to catch and jam on micro structure of the surface, and are thus able to generate adhesion on rough surfaces (Fig. 4). The linear-constrained microspine unit design consists of straight needles that can slide along channels in the substrate, slightly pressed by the soft normal springs to maintain contact against the surface. The unit accommodates 60 linearly-constrained spines. This microspine unit is designed specifically for heavy-duty applications, featured with large adhesion density, low contact compliance and good conformality to surface variation [24].

Contact friction of an individual spine engaged with an asperity can be described with the Coulomb model. However, when a group of spines interacts with terrain where the local curvature for each spine is randomly distributed, the overall contact property becomes complicated to model. It is inefficient to model many individual spines in contact because this requires detailed representation of the local contact geometry and kinematics of each spine. A more efficient method models 1D adhesion of a spine unit probabilistically based on empirical contact information of a single spine, which can then be extended to a 3D adhesion model that describes the adhesion profile over all loading directions (limit surface) of a spine unit.

The empirical data for a single spine contact includes maximum forces (150 data points per loading direction) that the spine can withstand before slipping, as measured by a force sensor. These data are described in more detail in [24]. The 3D limit surface (5 is derived based on how the adhesion degrades as the loading angle increases (away from the surface) due to decreasing number of usable asperities and increasing probability of non-spine-tip contact. With the assumption that all asperities are IID, the overall adhesion  $F$  at any 2D loading angle (x-z plane) can be computed with the integral over all the usable asperity slopes  $\psi$ :

$$F(\phi) = \frac{\int_{\psi_{\min}(\phi)}^{\psi_{\max}(\phi)} C_i(\psi, \beta) C_c(\phi, \beta) d\psi}{\int_{\psi_{\min}}^{\psi_{\max}} C_i(\psi, \beta) C_c(0, \beta) d\psi} F(0) \quad (11)$$

where  $\phi$  is the loading angle from surface tangential ( $x$ -axis),  $\beta$  is inclination angle of the spine.  $C_i$  and  $C_c$  are decay

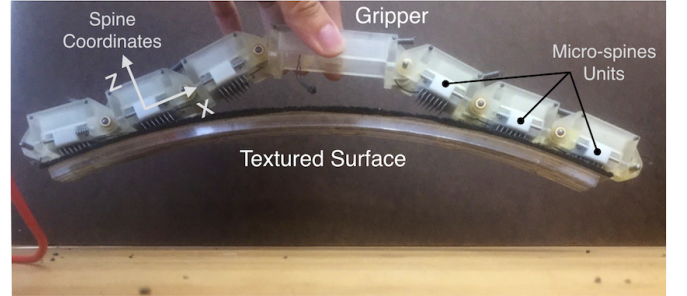


Fig. 6. Experiments equip a passive gripper with microspine units, which is lifted at the base to grasp a curved plate covered with roofing shingles. Different gripper configurations and surface curvatures are tested.

factors due to non-spine-tip contact and spine slip along sliding channel. The range of slopes  $[\psi_{\min}, \psi_{\max}]$  and maximum loading angle  $\phi_{\max}$  can be estimated empirically. When considering 3D cases, the only parameter changes from 2D is the equivalent spine inclination angle. With polar coordinate  $(\phi, \theta)$  to denote the loading direction where  $\theta$  represents the loading angle projected to the surface plane (x-y plane), the equivalent inclination angle  $\beta'$  becomes:

$$\beta'(\theta) = \arcsin(\sin \beta \cdot \cos \theta) \quad (12)$$

which substitutes into equation (11) to compute the 3D limit surface for  $z \leq 0$  (adhesion). Friction between spine substrate and contact surface is then included to model the other half of the limit surface. More details and empirical validation are available in Wang et al 2017 [25].

The limit surface is shown in Fig. 5. Any possible force vector created by the spine unit should stay within this boat-shaped hull. This non-convex surface shows that the spine unit adhesion degrades as the loading direction points more towards the surface normal (away from the contact surface) and eventually disappears. Due to the inclination of the spines, which are not perpendicular to the contact surface, there exists an optimal shear loading direction tangential to the surface, which is chosen as the x axis.

### B. Microspine grippers

We test our method with three assemblies: two spring-loaded opposed units (2OU), a passive two-finger gripper with 3 linearly-constrained units per finger (2FG), and a four-finger hand with actuation capabilities (4FH). The two-finger gripper is used for the physical experiments; the 4FH has not yet been experimentally validated as of time of writing.

### C. Numerical Experiments

a) *Contact and wrench space modeling*: Each microspine unit that touches the object is considered “enabled.” When enabled, the entire unit is assumed to make solid contact with the object, and is represented as a rectangular patch with four point contacts at the vertices. At each vertex, we define a force limit surface equal to 1/4 the empirical force limit surface of the entire unit; this allows for a patch to resist torques, both parallel to and perpendicular to the contact normal.

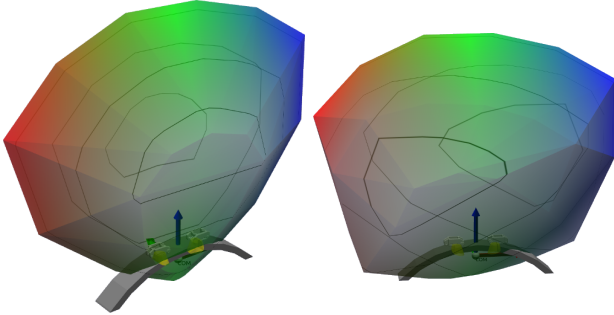


Fig. 7. 3D slices of the wrench space of the two-opposed unit (2OU) example lifting a curved object. Left:  $(f_x, f_y, f_z)$  slice. Right:  $(f_x, t_y, f_z)$  slice. Color indicates increasing  $x$  coordinate. Level sets are indicated on the  $y$  coordinate.

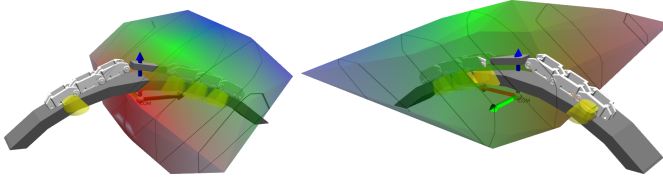


Fig. 8. 3D slices of the wrench space of the passive two-finger gripper (2FG) example in the distal-all phalanges (D-PMD) contact condition. Top:  $(f_x, f_y, f_z)$  slice. Bottom:  $(f_x, t_y, f_z)$  slice, rear view.

The admissible force volume is decomposed into 4 convex polyhedra, with 101, 91, 52, and 52 vertices, respectively.

To illustrate the space of external wrenches we use the formulation of (6). These images are generated by sampling wrench directions from a 3D subspace of the wrench space using a regular sampling on a sphere. Below we use one of two 3D subspaces of the 6D wrench space: either (1) forces through the center of mass ( $f_x, f_y, f_z$ ), or (2) forces along the x-z plane as well as torques about the normal ( $f_x, t_y, f_z$ ).

*b) Opposed Units (2OU):* The 2OU device combines two opposed units, spines pointing inward, connected via a spring-loaded slide. When contact is made between the units and a rough object, and the spring is loaded to apply an inward force, the spines engage the object. This allows for each unit to apply adhesive forces, and due to the admissibility of tangential shear forces, it can also apply stronger effective friction during compressive contact than would otherwise be possible.

Fig. 7 illustrates the limit surface of the assembly, which is boat-shaped and elongated in the shear direction. Its  $z$  coordinate also passes below 0, which indicates the ability to resist downward pulling forces with adhesive contact forces. It can also resist large upward forces with large effective friction.

*c) Passive Two-Finger Gripper (2FG):* The 2FG has a spine unit per phalanx and three phalanges per finger (Fig. 6). The phalanges are passive, being connected with bearing-supported pin joints to reduce joint friction, with no springs or tendons to apply torque. As a result, its admissible contact forces are highly limited because buckling would occur unless the net torque about the joint axis is low. As a result, torque constraints (5) are often the limiting factors. In contrast, 2OU and 4FH can exert active joint torques via springs, joint pulleys, and/or tendons. In these cases the primary limiting factors are shear friction and adhesion limits.

We calculated wrench spaces for this device in different

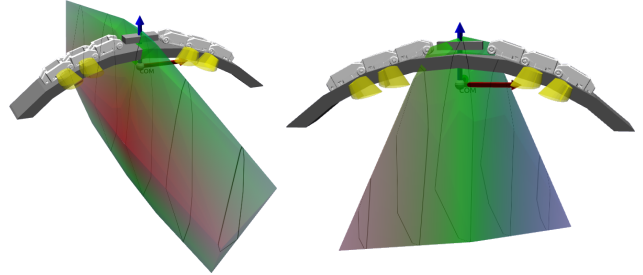


Fig. 9. 3D slices of the wrench space of the passive two-finger gripper (2FG) example in the medial-distal-medial-distal (MD-MD) contact condition. Left:  $(f_x, f_y, f_z)$  slice. Right:  $(f_x, t_y, f_z)$  slice.

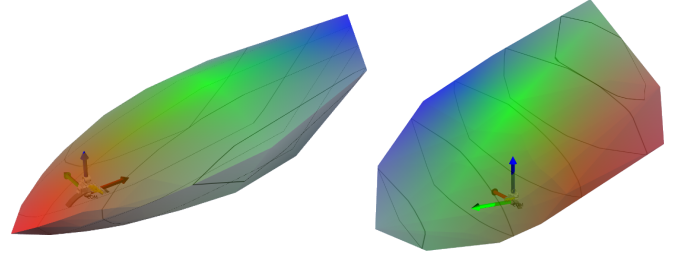


Fig. 10. 3D slices of the wrench space of the four-finger hand (4FH) example in the parallel (Par.) finger configuration. Top:  $(f_x, f_y, f_z)$  slice. Bottom:  $(f_x, t_y, f_z)$  slice, rear view.

configurations. The masses of each link and the object were measured within 1 g accuracy, while centers of mass were estimated relatively coarsely. Joint friction is assumed to be 0.01 Nm. Configurations are denoted by the initials of the left and right phalanges in contact (P: proximal, M: medial, D: distal), separated by a dash, e.g., D-D, MD-MD, D-PMD, etc.

In general, the gripper can resist stronger loads in the  $y$  direction because it is parallel to the passive joint axes and thus demands less joint friction to keep the links stationary. Also, the wrench space grows with more phalanges in contact. Fig. 8 and 9 illustrate two slices of the wrench spaces for the D-PMD and MD-MD configurations, respectively. The D-PMD configuration is able to support diagonal loads and stronger wrenches about the  $y$  axis, since it can recruit 3 spine units to resist rightward shear. The MD-MD configuration is able to support stronger downward forces because its symmetry allows shear forces to counterbalance one another. However, it is poor at resisting torques.

*d) Four Finger Hand (4FH):* The 4FH (SpinyHand) device is illustrated in Fig. 1. We investigate the differences in applicable wrenches when two outer fingers rotate between

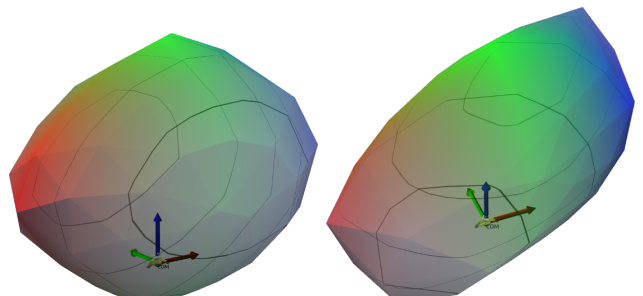


Fig. 11. 3D slices of the wrench space of the four-finger hand (4FH) example in the opposed (Opp.) finger configuration. Top:  $(f_x, f_y, f_z)$  slice. Bottom:  $(f_x, t_y, f_z)$  slice.

TABLE I  
TIMING RESULTS

Problem	Config.	# units	# CPs	Eq. (avg [min,max])	Eq. SCIP (avg [min,max])	Opt. (avg [min,max])	# CP (avg [min,max])
2OU	—	2	8	25ms [21ms,72ms]	254ms [242ms,266ms]	38ms, [29ms,288ms]	1.1 [1,11]
2FG	D-D	2	8	55ms [49ms,111ms]	527ms [270ms,1.2s]	294ms [29ms,6.7s]	10 [1,271]
2FG	D-MD	3	12	108ms [51ms,336ms]	2.7s [792ms,9.2s]	3.6s [41ms,79.5s]	84 [1,2246]
2FG	D-PMD	4	16	366ms [82ms,3.1s]	24s [536ms,5m+]	8.3s [57ms,178s]	154 [1,3392]
2FG	MD-MD	4	16	461ms [73ms,23.8s]	50s [492ms,5m+]	4.1s [80ms,14.9s]	61 [1,262]
2FG	MD-PMD	5	20	180ms [94ms,1.0s]	53s [640ms,5m+]	10s [87ms,267s]	159 [1,4276]
2FG	PMD-PMD	6	24	185ms [136ms,288ms]	2.5s [739ms,20s]	12s [149ms,260s]	92 [1,2272]
4FH	Par	12	48	321ms [298ms,396ms]	2.8s [1.8s,15s]	2.6s [226ms,28s]	10 [1,271]
4FH	Opp	12	48	581ms [353ms,815ms]	1.8s [1.6s,2.5s]	5.8s [574ms,69s]	9.3 [1,116]

a parallel (Par.) and opposed (Opp.) configurations. Each joint is assumed to be able to exert a torque of 10 Nm. The fingers are slightly curved as though gripping a rock, and all 12 finger units are assumed to be engaged. Fig. 10 and Fig. 11 the wrench spaces for Par. and Opp., respectively. Par. can withstand heavy forces and torques in the finger-oriented direction because each unit is able to apply optimal shear. Opp. can better withstand downward loads because opposed shear forces are able to produce a net adhesion.

#### D. Physical Experiments

We compare the predictions of our method with the physical experiments of Fig 6. A set of laser-cut acrylic objects with different curvature are fabricated, then covered with roofing shingle to create a rough texture. In each test, the 2FG gripper is firstly pre-shaped and pushed against the object so several phalanges make contact. It is then lifted up by the base to grasp the surface passively: as the gripper moves upwards, the phalanges bend towards and “push” against the surface due to gravity, applying shear and adhesive forces (Fig. 6). Then, the gripper is slowly reoriented in various directions by hand until the object falls.

For each experiment we posed the simulated gripper manually to match the physical gripper and observed which phalanges made contact with the object. Fig. 12 shows that the method was able to accurately predict the angle of slip onset in 11/14 slip events. Fig. 13 shows the failure cases. In the first two, the left distal phalanx catches the tip of the object, and this contact is not included in our model. In the third, the left proximal link makes partial contact, and eventually separates. Our method fails to predict separation at this point because it (overconfidently) determines that the proximal and medial joints admit opposed forces that can produce net adhesive force. Excluding the proximal link leads to an accurate prediction of slip onset.

#### E. Implementation Notes and Running Time

Our algorithms are implemented in the Python language, with CVXOPT as the convex program solver [1]. All experiments are performed on a single core of an 8 core Intel i7 processor. Sparse matrices are used for all linear inequalities. Some overhead may be reduced by implementation in a compiled language, but in our experiments over 80% of running time is spent inside the compiled convex program solver.

Experiments in Table I test equilibrium for 72 gravity directions in the range [0°, 360°]. Directional wrench optimization

experiments are conducted for 135 directions in a sphere of forces through the object’s center of mass. The leftmost columns give the problem, configuration, number of units, and number of contact points. Average, minimum, and maximum equilibrium testing time (Eq.), optimization time (Opt.), and number of convex program solves (# CP) are given in the remaining columns. We observe a few notable trends:

- Average running time scales modestly in the number of contact points.
- Worst-case running time is 1–2 orders of magnitude worse than average.
- Worst-case scenarios happen rarely.
- Optimization is approximately an order of magnitude slower than feasibility testing.

The cases that exhibit worst-case behavior tend to be on the border between feasibility and infeasibility, which cause the solver to oscillate between combinations of integer solutions.

We compare against the MILP solvers in SCIP v3.2.1 [10] and Gurobi 7.0.2 [12]. Experiments show that SCIP is approximately 5–10x times slower than our algorithm when solutions were easily found. However, SCIP becomes extraordinarily slow in the worst case as the number of units grows. For example, in the D-PMD problem, for some directions of external load, SCIP was unable to find a solution after 1 hour of computation time. Hence, when generating the SCIP timing column (Eq. SCIP) all runs were capped at 5 minutes. In each row where the cap was reached (D-PMD, MD-MD, and MD-PMD), 5–10% of runs failed. Gurobi performed with similar trends as SCIP, but was 1.5–4 times slower.

#### V. HIERARCHICAL EQUILIBRIUM PREDICTION

We now proceed to the more complex problem of predicting the equilibrium of a robot’s body with multiple hands in contact with rough terrain. It is possible to use the method developed above to simply treat the robot as a rigid body, and aggregate the contact units of all hands into a large MILP. However, this proves to be too computationally expensive for applications like motion planning, taking up to 10 s per equilibrium test and 50 s per optimization.

To address this challenge, we developed a hierarchical approach that learns the wrench space for each hand at a particular grip, and then treats each hand as a “unit” for body equilibrium testing. Fig. 14 displays the SpinyHand in four prototypical grips. We use our method to generate wrench spaces for each grip which are then used for equilibrium testing of various body postures of the RoboSimian. This

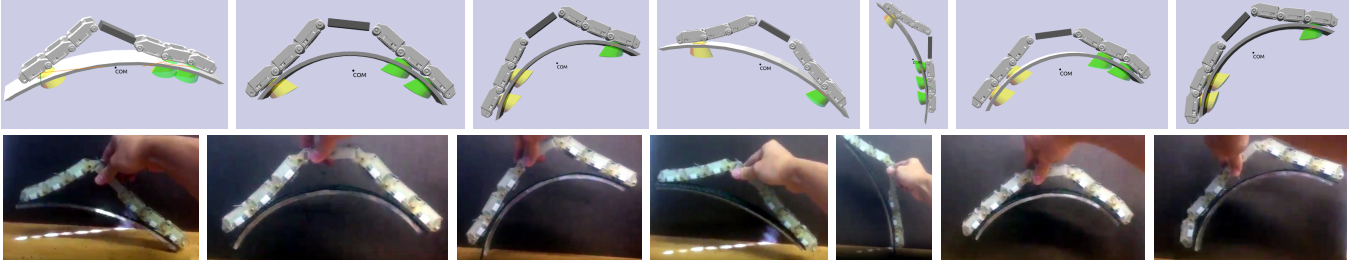


Fig. 12. Experiments exhibiting close agreement between predicted and actual onset of slip.



Fig. 13. Two experimental runs with inaccurate predictions. Left group: the model predicted the first slip event early (middle) and did not predict the final slip (right). Right group: the model did not predict the final slip (left).

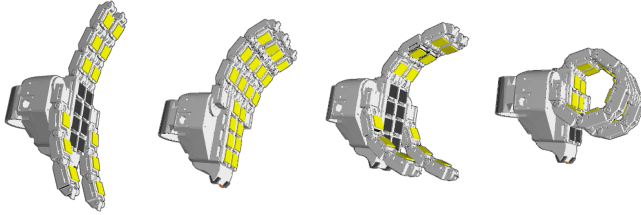


Fig. 14. Four grips of the SpinyHand that are evaluated in experiments (opposing, unified, pinch, and power). The contact units that are assumed to engage the terrain are highlighted.

is analogous to a human climber who learns the maximum loading characteristics of different grips through trial and error, and then uses that information to predict whether certain body movements are feasible.

To learn these spaces, we use the method presented above to compute an approximate wrench space of a hand in a nominal frame, and a given finger pose and contact configuration. The “empirical” testing is simulated in that we extremize loading wrenches in different directions to obtain inner and outer wrench limit surfaces. After an extensive precomputation, the method runs in sub-second time, and is fast enough to compute support polygons within a few seconds.

#### A. Learning Admissible Wrench Spaces

The method begins by approximating the *admissible wrench space* for each hand in a given finger and contact configuration (referred to as a *grip G*). The admissible wrench space  $W_G$  is a set in  $\mathbb{R}^6$  that describes the applicable (coupled) forces and torques  $w = (f, m)$  that the hand can apply.  $W_G$  is defined relative to some reference frame attached to the hand’s palm. If the pose of the hand’s palm is  $T_H \in SE(3)$ , then the transform from local wrenches to world-space wrenches is given by a

linear transform defined by the  $6 \times 6$  matrix

$$\tilde{T}_H \equiv \begin{bmatrix} R_H & 0 \\ [t_h] & R_H \end{bmatrix} \quad (13)$$

where  $R_H$  and  $t_H$  are the rotation and translation components of  $T_H$ . Hence, the set of admissible world-space wrenches applicable by the hand is given by

$$\{\tilde{T}_H w \mid w \in W_G\}. \quad (14)$$

To calculate the 6-D wrench space  $W_G$  for a given grip, we opt for a sampling approach rather than an exact representation, since the exact set is intractably complex. Our approach obtains samples on the wrench limit surface by extremizing along a wrench space ray passing through the origin. Specifically, we sample directions  $\hat{w} \in \mathbb{R}^6$  and calculate the maximized extent  $d$  by solving (6) with a MILP. The wrench  $d\hat{w}$  then lies on  $\partial W_G$ .

It would be extremely computationally expensive to perform convex decompositions of 6D sets as we have done for 3D admissible force volumes in Section III-F. Luckily, we make the observation that *non-convex wrench spaces are rare*. In fact, the small number of non-convex wrench spaces that we have encountered in our experiments are nearly convex, with the least concave having a boundary concavity metric of 0.01 (in units of a combination of N and N·m). In general, pockets (concavities) shrink in volume as the number of contact patches grows. This is a result of the Shapley-Folkman-Starr theorem and its extensions [21], which state that the difference between the Minkowski sum of nonconvex sets and the sum of their convex hulls shrinks as more sets are summed. The feasible equilibrium set (3) is the intersection of a Minkowski sum of linearly transformed admissible force volumes and a hyperplane; hence, the convex approximation is a good one.

Another important aspect of the problem is the directional sampling distribution, since for best approximation accuracy

we would like to sample evenly from the surface  $\partial W_G$ . An approximation is to generate point contact forces  $f_1, \dots, f_k$  each uniformly from a multivariate Gaussian, and then calculate the wrench map  $\hat{w} = Wf$ . In other words, we sample  $\hat{w} \sim N(0, WW^T)$ .

### B. Equilibrium Test

When the body is in contact with the terrain with  $k$  hands  $H_1, \dots, H_k$  with local wrench spaces  $W_{G_1}, \dots, W_{G_k}$  and transforms  $\tilde{T}_{H_1}, \dots, \tilde{T}_{H_k}$  respectively, equilibrium can be tested with the following problem:

$$\text{Find } w_1, \dots, w_k \in \mathbb{R}^6$$

such that

$$w_g = \sum_{j=1}^k \tilde{T}_{H_j} w_j \quad (15)$$

$$w_j \in W_{G_j} \text{ for all } j = 1, \dots, k.$$

The first condition enforces equilibrium with the gravity wrench  $w_g$  and the second ensures wrench feasibility. The wrench exerted by the gravity force relative to the origin is

$$w_g \equiv \begin{bmatrix} Mg \\ c \times Mg \end{bmatrix} \quad (16)$$

where  $M$  is the total mass of the robot,  $g$  is the gravity vector, and  $c$  is the robot's center of mass.

To solve (15) as an LP the condition  $w_j \in W_{G_j}$  must be encoded. Convex polytopes can be represented in two dual forms: the *V-representation* (V-*rep*), which represents the volume as the convex hull of a set of vertices, and the *H-representation* (H-*rep*), which represents the volume as a set of intersected halfspaces. In the former,  $W_G$  is represented by a set of  $N$  extreme wrenches  $\{v_1, \dots, v_N\}$  with each  $v_i \in \mathbb{R}^6$ , and the admissible volume is defined by

$$W_G = \text{hull}(\{v_1, \dots, v_N\}). \quad (17)$$

In an H-*rep*, the facets of  $W_G$  are represented by rows of an  $N \times 6$  matrix  $A$  and a column vector  $b \in \mathbb{R}^N$  that define the set:

$$W_G = \{w \mid Aw \leq b\}. \quad (18)$$

The advantage of V-*reps* is that extremizing a wrench in a given direction gives a vertex of the polytope, which is the natural form of our admissible wrench spaces. Moreover, the convex hull of a set of vertices in 6D typically has orders of magnitude more facets than vertices. The main advantages of the H-*rep* are efficient point inclusion testing and more direct encoding in linear / quadratic programs. If  $W_{G_j}$  is an H-*rep*, we encode the halfplane constraints:

$$Aw_j \leq b \quad (19)$$

into the optimization. If  $W_{G_j}$  is a V-*rep*, we augment the problem with coefficients  $c_1, \dots, c_N$  and the convex hull constraints

$$\sum_{i=1}^N c_i v_i = w_j, \quad \sum_{i=1}^N c_i = 1, \quad (20)$$

$$c_i \geq 0 \text{ for all } i = 1, \dots, N.$$

### C. Support Polygon Calculation

The support polygon for an robot in contact with a fixed terrain characterizes the set of center of mass positions that admit equilibrium with gravity. Specifically, a robot is at equilibrium if its center of mass lies within an infinite vertical generalized cylinder, with a constant cross-section in the  $x$ - $y$  plane [7]. The support polygon is the cross section of this cylinder. In flat or nearly-flat terrain, this is identical to the convex hull of the support points, but in highly uneven terrains the support polygon can be entirely different.

With each contact's wrench space a convex polytope, calculating the support polygon is a polytope intersection problem in which we intersect the polytope of possible resultant wrenches on the robot with the plane of wrenches induced by possible gravity wrenches at different centers of mass. Specifically, this is the set of all center of mass positions  $x, y$

$$\{(x, y) \mid w_{x,y} \in \bigoplus_{j=1}^k \tilde{T}_{H_j} W_{G_j}\} \quad (21)$$

with the gravity wrench at center of mass position  $(x, y, \cdot)$  defined as

$$w_{x,y} \equiv \left[ \begin{bmatrix} x \\ y \\ 0 \end{bmatrix} \times mg \right] \quad (22)$$

where  $m$  is the mass of the robot. Note that this is a linear function of  $x$  and  $y$ .

To approximate the boundary of (21) we extremize over wrench directions in the  $x$ - $y$  plane. Because the support polygon is convex in our case, we obtain slightly better results by maximizing the dot product of the resultant wrench in a direction  $d_{x,y}$  on the  $(x, y)$  plane rather than constraining the wrench to a ray. Specifically, we solve

$$\max_{w_1, \dots, w_k, x, y} d_{x,y}^T \begin{bmatrix} x \\ y \end{bmatrix} \quad \text{such that} \quad (23)$$

$$xw_{1,0} + yw_{0,1} = \sum_{j=1}^k \tilde{T}_{H_j} w_j$$

$$w_j \in W_{G_j} \text{ for all } j = 1, \dots, k$$

The point  $(x, y)$  is then a point on the boundary of the support polygon. We perform this optimization for a number of directions  $d_{x,y}$  and then calculate the convex hull.

### D. Inner and Outer Bounding

With admissible wrench spaces sampled at thousands of vertices, equilibrium prediction becomes impractically expensive. One of our example grasp shapes yielded a polytope of 6,615 vertices and 1,289,480 facets. Predicting equilibrium for a four-hand posture took more than three hours for both V- and H-*reps*.

Instead, we take an approach similar to the adaptive equilibrium test method [7] that allows us to trade off between accuracy and computation speed using inner and outer bounds. This lets us approximate any  $W_G$  to a given level of accuracy. We

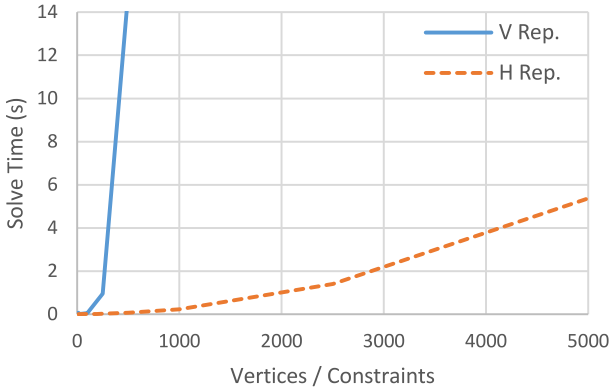


Fig. 15. Equilibrium prediction times for a four-hand problem as the complexity of the representation of the hand wrench space grows. Both vertex (V Rep.) and halfspace (H Rep.) representations are given.

maintain bounding polytopes  $W_G^{inner}$  and  $W_G^{outer}$  satisfying  $W_G^{inner} \subseteq W_G \subseteq W_G^{outer}$ , and which have lower complexity than  $W_G$ . If the solver can find a solution with inner bounds, the robot is certainly in equilibrium. If it finds no solution with outer bounds, the robot is certainly not in equilibrium. If neither of these conditions holds, the equilibrium status is uncertain, and either a tighter bound could be explored, or the robot’s posture could be treated as unsafe. (Falls are often quite dangerous in climbing, so it would make sense to be more conservative and only allow postures for which an inner bound solution exists.)

To efficiently sample inner bounds, we use a V-rep constructed from a randomly chosen subset of extreme points. First, we pick a subset  $S$  uniformly at random from the original vertices  $\{v_1, \dots, v_N\}$ . Rather than use  $S$  directly as a new V-rep, we obtain a closer approximation to the volume by treating each element as a direction, and then extremizing. The inner V-rep includes extreme points  $v^*(\hat{w}) = \arg \max_{i \in \{1, \dots, N\}} \hat{w}^T v_i$  for each direction  $\hat{w} \in S$ . We ensure that the 0 vector is included in the sample. To sample outer bounds, we use an H-polytope constructed from random directions in the hypersphere  $\{\hat{w} \mid \|\hat{w}\| = 1\}$ , and for each extreme point we add the halfplane constraint  $\hat{w}^T x \leq \hat{w}^T v^*(\hat{w})$ .

### E. Simulation Experiments

We apply these techniques to a simulated Robosimian quadruped equipped with the Four Finger Hand for the purpose of climbing vertical and overhanging terrain. For each of the grips in Fig. 14, we sample several thousand points on the wrench limit surface. In our experiments, calculating the space for a single grip takes on the order of one to ten hours on a single core of an Intel i7 processor.

Fig. 15 illustrates the superlinear growth in equilibrium computation times with respect to representation complexity, for admissible wrench spaces represented as V-reps (inner) or H-reps (outer). Equilibrium prediction becomes expensive for even a few hundreds of vertices in V-rep form, while H-reps remain efficient at a few thousand constraints. However, the accuracy of each representation is not equivalent, because significantly more halfplanes than vertices are needed to obtain the same approximation accuracy.

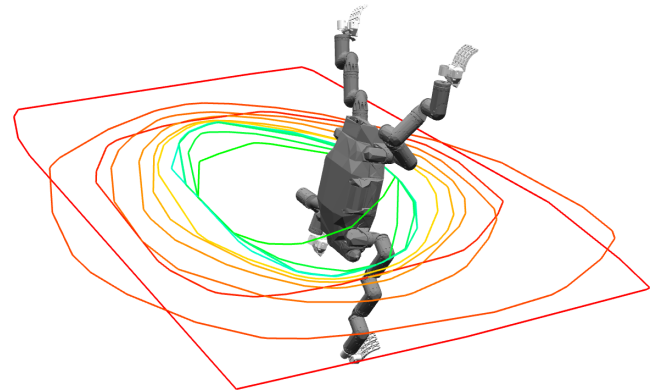


Fig. 16. Support polygons calculated for the Robosimian on a near-vertical terrain for different inner and outer approximations of the hand wrench spaces. Outer bounds are drawn in red to orange for increasing numbers of halfplanes ranging from 12 to 1,000, and the largest bound is for an axis-aligned bounding box. Inner bounds are drawn in green to cyan for increasing numbers of vertices from 25 to 250. (Best viewed in color)

The accuracy of equilibrium predictions vary with the quality of hand wrench space approximation. Fig. 16 illustrates inner and outer support polygons for different levels of approximation. Crude outer bounds (such as the outer bounding box) yield a very poor approximation to the true equilibrium region, which is between the cyan and orange polygons.

In our remaining experiments we choose 250 vertices for the inner approximation and 1,000 halfplanes for the outer approximation. With these settings, the equilibrium regions are computed in approximately 10 s for 32 evenly sampled extremization directions. The regions for different grips in an overhanging posture are shown in Figs. 17 and 18. The power grip admits the most freedom of movement, but can only be applied when the fingers can wrap entirely around a pole or branch. The parallel grip is second best, and the pinch grip is slightly better than the opposing grip. Interestingly, the pinch grip admits greater range of motion into the “wall” than the parallel grip, which indicates that the inward forces at the pinch help the hands avoid slipping away from the wall.

Fig. 18 illustrates similar configurations but with only one hand in contact. Here the equilibrium regions are much smaller. This reflects the increased physical difficulty of hanging backwards using a single hand rather than two hands, as is expected for human climbers. In fact, balance would not be feasible for the opposing, parallel, or pinch grips in the given configuration, and instead the center of mass should be shifted away from the wall. This strategy directs a greater inward force into the wall on the feet while using the hand as a pivot point; this is a strategy also used by human climbers to direct a greater share of load onto the feet.

## VI. CONCLUSION

We presented a method for computing the quasi-static stability of an assembly of contacts under empirically-determined limit surfaces that supports anisotropy, adhesion, and non-convexity. The mixed-integer linear programming (MILP) formulation is solved efficiently using a hierarchical convex decomposition and custom solver heuristics. Numerical tests

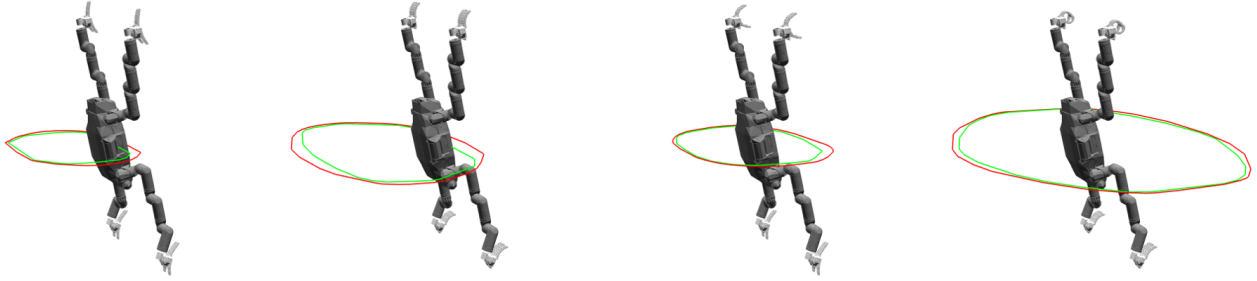


Fig. 17. Equilibrium regions for different grips in a two-handed, two-footed overhanging posture. The robot is tilted backward at approximately  $15^\circ$ , and the green equilibrium region denotes the inner approximation and the red denotes the outer approximation. From left to right: opposing grip; parallel grip; pinch grip for hands with feet in opposing grip; and power grip for hands with feet in parallel grip.

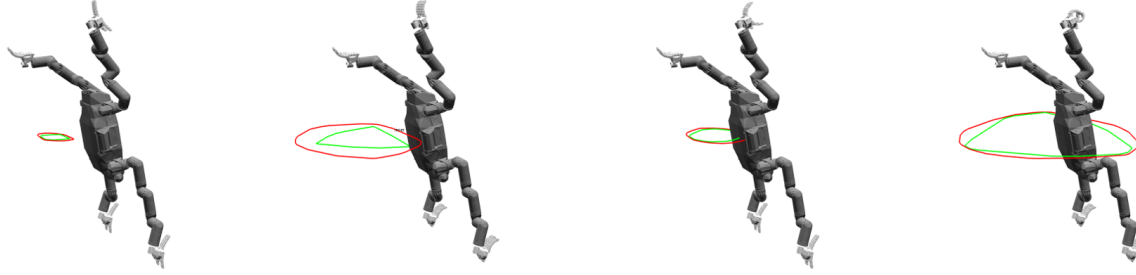


Fig. 18. Equilibrium regions for different grips in a one-handed, two-footed overhanging posture. From left to right: opposing grip; parallel grip; pinch grip for hand with feet in opposing grip; and power grip for hand with feet in parallel grip.

demonstrate that it works orders of magnitude faster than an off-the-shelf MILP solver, and empirical tests suggest close agreement with experiments on a 2 fingered gripper. This method is applied hierarchically to a microspine gripper to predict equilibrium conditions for a quadruped climbing robot, which suggests that our method can be used for choosing grips and postures during motion planning.

Several promising avenues for future work remain. First, the solver is not yet fast enough for real-time physics simulation, and perhaps warm-starting would help in the presence of temporal consistency. Second, we only test the notion of *weak equilibrium* — verifying the existence of admissible forces in the best-case — whereas the notion of *strong equilibrium* may lead to more accurate predictions [20]. Hysteresis and deformation should also be taken into account to characterize many contact phenomena of interest. Furthermore, the stochastic nature of microscopic surface features leads to variability in loading characteristics that is observed in empirical testing, and to properly handle stochasticity, new probabilistic methods would need to be developed.

#### ACKNOWLEDGMENTS

This work was supported by NSF NRI grant #1527826.

#### REFERENCES

- [1] M. S. Andersen, J. Dahl, and L. Vandenberghe. Cvxopt: A python package for convex optimization, version 1.1.5, 2012. URL <http://abel.ee.ucla.edu/cvxopt>.
- [2] A. T. Asbeck, S. Kim, M. R. Cutkosky, W. R. Provancher, and M. Lanzetta. Scaling hard vertical surfaces with compliant microspine arrays. *Int. J. Robotics Research*, 25(12):1165–1179, 2006. URL <http://dx.doi.org/10.1177/0278364906072511>.
- [3] D. Baraff. Fast contact force computation for nonpenetrating rigid bodies. In *Proc. 21st Annual Conf. Computer Graphics and Interactive Techniques, SIGGRAPH '94*, pages 23–34, New York, NY, USA, 1994. ACM. URL <http://doi.acm.org/10.1145/192161.192168>.
- [4] A. Bicchi and V. Kumar. Robotic grasping and contact: a review. In *IEEE Int. Conf. on Robotics and Automation*, volume 1, pages 348–353, 2000. doi: 10.1109/ROBOT.2000.844081.
- [5] S. P. Boyd and B. Wegbreit. Fast computation of optimal contact forces. *IEEE Trans. Robotics*, 23(6):1117–1132, Dec 2007. doi: 10.1109/TRO.2007.910774.
- [6] B. Brazey, R. Dahmouche, J.-A. Seon, and M. Gauthier. Experimental validation of in-hand planar orientation and translation in microscale. *Intel. Service Rob.*, 9(2):101–112, Apr. 2016. URL <http://dx.doi.org/10.1007/s11370-015-0183-0>.
- [7] T. Bretl and S. Lall. Testing static equilibrium for legged robots. *IEEE Trans. Robotics*, 24(4):794–807, Aug 2008. doi: 10.1109/TRO.2008.2001360.
- [8] A. Fakhari, M. Keshmiri, and I. Kao. Development of realistic pressure distribution and friction limit surface for soft-finger contact interface of robotic hands. *J. Intelligent & Robotic Systems*, 82(1):39–50, 2016. URL <http://dx.doi.org/10.1007/s10846-015-0267-2>.
- [9] N. Fazeli, R. Kolbert, R. Tedrake, and A. Rodriguez. Parameter and contact force estimation of planar rigid-bodies undergoing frictional contact. *Int. J. Robotics Research*, 36(13–14):1437–1454, 2017. URL <https://doi.org/10.1177/0278364917698749>.

- [10] G. Gamrath, T. Fischer, T. Gally, A. M. Gleixner, G. Hendel, T. Koch, S. J. Maher, M. Miltenberger, B. Müller, M. E. Pfetsch, C. Puchert, D. Rehfeldt, S. Schenker, R. Schwarz, F. Serrano, Y. Shinano, S. Vigerske, D. Weninger, M. Winkler, J. T. Witt, and J. Witzig. The scip optimization suite 3.2. Technical Report 15-60, ZIB, Takustr.7, 14195 Berlin, 2016.
- [11] S. Goyal, A. Ruina, and J. Papadopoulos. Limit surface and moment function descriptions of planar sliding. In *IEEE Int. Conf. on Robotics and Automation*, volume 2, pages 794–799, May 1989. doi: 10.1109/ROBOT.1989.100081.
- [12] Gurobi Optimization, Inc. Gurobi optimizer version 7.0.2, 2017. URL <http://www.gurobi.com>.
- [13] K. Hauser, S. Wang, and M. Cutkosky. Efficient equilibrium testing under adhesion and anisotropy using empirical contact force models. In *Robotics: Science and Systems*, 2017.
- [14] E. W. Hawkes, D. L. Christensen, E. V. Eason, M. A. Estrada, M. Heverly, E. Hilgemann, H. Jiang, M. T. Pope, A. Parness, and M. R. Cutkosky. Dynamic surface grasping with directional adhesion. In *IEEE/RSJ Int. Conf. on Intelligent Robotics and Systems*, pages 5487–5493, Nov 2013. doi: 10.1109/IROS.2013.6697151.
- [15] E. W. Hawkes, H. Jiang, and M. R. Cutkosky. Three-dimensional dynamic surface grasping with dry adhesion. *Int. J. Robotics Research*, 35(8):943–958, July 2016. URL <http://dx.doi.org/10.1177/0278364915584645>.
- [16] R. D. Howe and M. R. Cutkosky. Practical force-motion models for sliding manipulation. *Int. J. Robotics Research*, 15(6):557–572, 1996. URL <http://dx.doi.org/10.1177/027836499601500603>.
- [17] R. Kolbert, N. C. Dafle, and A. Rodriguez. Experimental validation of contact dynamics for in-hand manipulation. In *Int. Symp. Experimental Robotics*, 2016.
- [18] S. H. Lee and M. R. Cutkosky. Fixture planning with friction. *J. Engineering for Industry*, 113(3):320–327, Aug. 1991. doi: 10.1115/1.2899703.
- [19] C. Majidi, R. Groff, Y. Maeno, B. Schubert, S. Baek, B. Bush, R. Maboudian, N. Gravish, M. Wilkinson, K. Autumn, and R. Fearing. High friction from a stiff polymer using micro-fiber arrays. *Physical Review Letters*, 97(076103), Aug. 2006.
- [20] J. S. Pang and J. C. Trinkle. Stability characterizations of fixtured rigid bodies with coulomb friction. In *IEEE Int. Conf. on Robotics and Automation*, volume 1, pages 361–368, 2000. doi: 10.1109/ROBOT.2000.844083.
- [21] R. M. Starr. Quasi-equilibria in markets with non-convex preferences. *Econometrica*, 37(1):25–38, Jan. 1969.
- [22] D. E. Stewart. Rigid-body dynamics with friction and impact. *SIAM Review*, 42(1):3–39, 2000. URL <http://dx.doi.org/10.1137/S0036144599360110>.
- [23] P. Tiezzi and I. Kao. Modeling of viscoelastic contacts and evolution of limit surface for robotic contact interface. *IEEE Trans. Robotics*, 23(2):206–217, April 2007. doi: 10.1109/TRO.2006.889494.
- [24] S. Wang, H. Jiang, and M. R. Cutkosky. A palm for a rock climbing robot based on dense arrays of micro-spines. In *IEEE/RSJ Int. Conf. on Intelligent Robotics and Systems*, pages 52–59, 2016.
- [25] S. Wang, H. Jiang, and M. R. Cutkosky. Design and modeling of linearly-constrained compliant spines for human-scale locomotion on rocky surfaces. *Int. J. Robotics Research*, 36(9):985–999, 2017. URL <https://doi.org/10.1177/0278364917720019>.
- [26] K.-T. Yu, M. Bauza, N. Fazeli, and A. Rodriguez. More than a million ways to be pushed. a high-fidelity experimental dataset of planar pushing. In *IEEE/RSJ Int. Conf. on Intelligent Robotics and Systems*, pages 30–37, 2016.
- [27] J. Zhou, R. Paolini, J. A. Bagnell, and M. T. Mason. A convex polynomial force-motion model for planar sliding: Identification and application. In *IEEE Int. Conf. on Robotics and Automation*, pages 372–377, 2016.



**Kris Hauser** is an Associate Professor at Duke University with joint appointments in the Departments of Electrical & Computer Engineering and Mechanical Engineering and Materials Science. He received his PhD in Computer Science from Stanford University in 2008, bachelor's degrees in Computer Science and Mathematics from UC Berkeley in 2003, and was a postdoc at UC Berkeley. He joined the faculty of Indiana University from 2009–2014, where he started the Intelligent Motion Lab, and began his current position at Duke in 2014. He is a recipient of a Stanford Graduate Fellowship, Siebel Scholar Fellowship, Best Paper Award at IEEE Humanoids 2015, and an NSF CAREER award.



**Shiquan Wang** is founder and CEO of Flexiv Robotics Ltd. He received his PhD in Mechanical Engineering from Stanford University in 2017, and bachelors degrees in Mechatronic Engineering from Zhejiang University in 2012. He is a recipient of the Best Paper Award (safety, security and rescue robotics) at IEEE International Conference on Intelligent Robots and Systems 2016. His research focuses on human-scale robot locomotion and manipulation in complicated environment, which is related with dexterous hand design, grasping and manipulation, contact modeling and dynamic simulation, sensing and actuation system for legged and articulated robots.



**Mark R. Cutkosky** received the Ph.D. degree in mechanical engineering from Carnegie Mellon University, Pittsburgh, PA, USA, in 1985. He is the Fletcher Jones Professor in mechanical engineering at Stanford University, Stanford, CA, USA. His research interests include bioinspired robots, haptics and rapid prototyping processes. Dr. Cutkosky is a Fellow of the ASME and IEEE.